C. R. Mecanique 340 (2012) 721–730

Contents lists available at SciVerse ScienceDirect

Comptes Rendus Mecanique

www.sciencedirect.com

A dynamic sub-grid scale model for large eddy simulation of turbulent flows in a lid-driven cubical cavity

Nader Ben-Cheikh [a,*], Faycel Hammami [a], Antonio Campo [b], Brahim Ben-Beya [a]

[a] *Laboratory of Fluid Dynamics, Physics Department, Faculty of Science of Tunis, Campus Universitaire, 2092 El-Manar II, Tunisia*
[b] *Department of Mechanical Engineering, The University of Texas at San Antonio, San Antonio, TX 78249, USA*

ARTICLE INFO

Article history:
Received 12 July 2012
Accepted after revision 1 October 2012
Available online 22 October 2012

Keywords:
Turbulence
Lid-driven cubical cavity
Incompressible fluid
Large eddy simulation
WALE model
Dynamic sub-grid scale

ABSTRACT

This work undertakes a numerical study of turbulent incompressible flows in lid-driven cubical cavities using Large Eddy Simulation and two sub-grid scale models, i.e., the WALE (Wall-Adapting Local Eddy-viscosity) model and the corresponding dynamic sub-grid model (DSGS). In the process of using DSGS, an optimal value of constant C_W of the WALE model was determined for a pre-set Reynolds number $Re = 10^4$. The computed numerical results showed very good agreement with those Direct Numerical Simulation (DNS) results and with the experimental measurements found in the literature. Optimal values of C_W were determined afterwards with the DSGS model and they were proposed for the analysis of higher Reynolds number turbulent flows. At the end, a power law correlation between C_W and Re was proposed for the range $10^4 \leqslant Re \leqslant 3 \times 10^4$.

© 2012 Académie des sciences. Published by Elsevier Masson SAS. All rights reserved.

1. Introduction

Numerical simulations of turbulent flows are of great interest in a multitude of engineering applications in industry. It is well known that for high Reynolds number turbulent flows, the extended range of turbulent scales is of concern. The small scales are of the order of the Kolmogorov length scale and the largest scales are of the order of the domain dimensions. Direct Numerical Simulation (DNS) cannot solve high Reynolds turbulent flows due to the large amount of computational information generated by the large range of scales. Owing to this drawback, DNS is normally restricted to low and moderate Reynolds number flows.

Another approach capable of predicting turbulent flows is the Reynolds Averaged Navier–Stokes (RANS), based on the Reynolds decomposition of the instantaneous flow variables into a mean and fluctuating components. During the last three decades, many researchers have embraced the RANS avenue as an alternative to simulate a variety of turbulent flows [1–4]. The disadvantage inherent to the RANS turbulence model stems from the fact that the turbulent fluctuations are eliminated by means of a time averaging process during which all the spectra effects are lost.

The Large Eddy Simulation (LES) methodology introduced by Smagorinsky [6] is another tool to simulate turbulent flows [5]. LES, situated between highest degrees of DNS and RANS, is expressed by the partition of the large eddies structures and sub-grid scales structures using a grid filter. Large-scale flow motions are explicitly computed, while small-scale flow motions are modeled with a sub-grid scale (SGS) model. LES is superior to DNS in terms of computational cost, and better than RANS in terms of accuracy and data availability.

Several SGS models have been utilized by a group of researchers: Smagorinsky's model [6], the dynamic SGS model initially proposed by Germano et al. [7] and reformulated by Lilly [8], the WALE model developed by Nicoud and Ducros [9]. In addition, other relevant SGS models can be found in Refs. [5,10,32,33].

* Corresponding author.
E-mail address: nader_bc@yahoo.fr (N. Ben-Cheikh).

1631-0721/$ – see front matter © 2012 Académie des sciences. Published by Elsevier Masson SAS. All rights reserved.
http://dx.doi.org/10.1016/j.crme.2012.10.001

In this work, we undertake the formulation, implementation and application of a numerical algorithm for three-dimensional turbulent flows in a lid-driven cubical cavity at relatively high Reynolds number. The adopted methodology is based on the finite volume method, coupled with a full-multigrid acceleration and LES. A computational code to simulate transient, incompressible, three-dimensional flows was developed [11,12] using the projection method [13]. Herein, two different SGS models were implemented, namely the WALE model [9] and the dynamic model [5,14].

The three-dimensional flow in a lid-driven cubical cavity has been studied experimentally [15,16] and numerically [17–22]. Statistical studies on the mean velocities, turbulence intensities and Reynolds stresses are performed and compared with those obtained numerically and experimentally by other authors. The model and methodology are first validated for $Re = 10^4$. Then, a correlation between the optimal constant C_W that appears in the WALE SGS model is determined and proposed for the range $10^4 \leqslant Re \leqslant 3 \times 10^4$.

2. Governing equations

2.1. Filtered equations

The unsteady Navier–Stokes equations for incompressible flows are:

$$\frac{\partial u_i}{\partial t} = 0 \tag{1}$$

$$\frac{\partial u_i}{\partial t} + \frac{\partial (u_i u_j)}{\partial x_j} = -\frac{1}{\rho}\frac{\partial p}{\partial x_i} + \nu \frac{\partial^2 u_i}{\partial x_j \partial x_j} \tag{2}$$

where u_i, p, ρ, and ν denote the velocity, the pressure, the density and the kinematic viscosity, respectively.

The LES equations are obtained by applying a filtering operation. The definition of a filtered variable is defined by:

$$\bar{f}(\vec{r}, t) = G * f(\vec{r}, t) = \iiint_V G\left(\left|\vec{r} - \vec{r'}\right|\right) f\left(\vec{r'}, t\right) \mathrm{d}\vec{r'} \tag{3}$$

where V is the volume of filtering and G is the filter function. After filtering Eqs. (1)–(2), the LES continuity and momentum equations take the form:

$$\frac{\partial \bar{u}_i}{\partial t} = 0 \tag{4}$$

$$\frac{\partial \bar{u}_i}{\partial t} + \frac{\partial (\bar{u}_i \bar{u}_j)}{\partial x_j} = -\frac{1}{\rho}\frac{\partial \bar{p}}{\partial x_i} + \nu \frac{\partial^2 \bar{u}_i}{\partial x_j \partial x_j} - \frac{\partial \tau_{ij}}{\partial x_j} \tag{5}$$

where the sub-grid scale stresses are given by:

$$\tau_{ij} = \overline{u_i u_j} - \bar{u}_i \bar{u}_j \tag{6}$$

Invoking the Boussinesq approximation, the SGS stresses are related to the eddy viscosity ν_T and the large scale strain rate tensor $\bar{S}_{ij}$ by means of the following expression:

$$\tau_{ij} - \frac{1}{3}\tau_{kk}\delta_{ij} = -2\nu_T \bar{S}_{ij} = -\nu_T \left(\frac{\partial \bar{u}_i}{\partial x_j} + \frac{\partial \bar{u}_j}{\partial x_i}\right) \tag{7}$$

2.2. WALE sub-grid scale model

Nicoud and Ducros [9] developed an advanced sub-grid scale model that takes into consideration both the strain and the rotation rate of the smallest resolved turbulent fluctuations. Taken information from DNS, Wray and Hunt [23] stated that the energy is concentrated in the streams and energy dissipation is significant in eddies and convergence zones. Incontestably, the common Smagorinsky model does not justify the contribution of the latter, which are zones where vorticity predominates irrotational strain. The model developed by Nicoud and Ducros [9] has two main advantages: (1) the viscosity tends to zero (of order $O(y^3)$) in the vicinity of a wall and (2) the viscosity does not need information for the position and direction of the wall. This last characteristic is especially meaningful when dealing with complex geometries and/or unstructured grid. For this particular model, named WALE (Wall-Adapting Local Eddy-viscosity), the eddy viscosity ν_T is expressed by:

$$\nu_T = (C_W \Delta)^2 \frac{\overline{OP_1}}{\overline{OP_2} + \varepsilon} = (C_W \Delta)^2 |\bar{N}_{ij}| \tag{8}$$

where C_W is the WALE constant model, Δ is the characteristic length scale representing the cell size, and $\varepsilon = 10^{-6}$. Besides, the other participating quantities are:

$$\overline{OP_1} = \left(S^d_{ij} S^d_{ij}\right)^{\frac{3}{2}}, \qquad \overline{OP_2} = (\overline{S_{ij}}\,\overline{S_{ij}})^{\frac{5}{2}} + \left(S^d_{ij} S^d_{ij}\right)^{\frac{5}{4}} \tag{9}$$

in which

$$S_{ij}^{d} = \frac{1}{2}\left(\bar{g}_{ij}^{2} + \bar{g}_{ji}^{2}\right) - \frac{1}{3}\delta_{ij}\bar{g}_{kk}^{2}, \quad \bar{g}_{ij} = \frac{\partial \overline{u_i}}{\partial x_j} \tag{10}$$

In reference to isotropic or weakly anisotropic grids, the magnitude of Δ is computed through $\Delta = (\Delta x \Delta y \Delta z)^{1/3}$ as assumed by Deardorff [24]. Owing that the present study revolves around anisotropic grids, Deardorff's form was corrected incorporating the proposition suggested by Scotti et al. [25].

2.3. Dynamic SGS model

Germano et al. [14] presented a dynamic SGS model (DSGS), wherein the model coefficient is calculated during the simulation relying on the application of two different filters. In addition to the grid filter G, a test filter $\widehat{G}$ is applied. The test filter width $\widehat{\Delta}$ is larger than the grid filter width Δ, usually $\widehat{\Delta} = 2\Delta$. First, the grid filter and the test filter are applied to the momentum equation (2):

$$\frac{\partial \bar{\bar{u}}_i}{\partial t} + \frac{\partial(\bar{\bar{u}}_i \bar{\bar{u}}_j)}{\partial x_j} = -\frac{1}{\rho}\frac{\partial \bar{\bar{p}}}{\partial x_i} + \nu \frac{\partial^2 \bar{\bar{u}}_i}{\partial x_j \partial x_j} - \frac{\partial T_{ij}}{\partial x_j} \tag{11}$$

where T_{ij} represent the sub-test stresses given by:

$$T_{ij} = \widehat{\tau}_{ij} + \widehat{\overbrace{\bar{u}_i \bar{u}_j}} - \bar{\bar{u}}_i \bar{\bar{u}}_j \tag{12}$$

The test filter is then applied to the filtered equation (5):

$$\frac{\partial \bar{\bar{u}}_i}{\partial t} + \frac{\partial(\bar{\bar{u}}_i \bar{\bar{u}}_j)}{\partial x_j} = -\frac{1}{\rho}\frac{\partial \bar{\bar{p}}}{\partial x_i} + \nu \frac{\partial^2 \bar{\bar{u}}_i}{\partial x_j \partial x_j} - \frac{\partial \widehat{\tau}_{ij}}{\partial x_j} - \frac{\partial L_{ij}}{\partial x_j} \tag{13}$$

$$\text{with } L_{ij} = \widehat{\overbrace{\bar{u}_i \bar{u}_j}} - \bar{\bar{u}}_i \bar{\bar{u}}_j = T_{ij} - \widehat{\tau}_{ij} \tag{14}$$

Let us model both τ_{ij} and T_{ij} by the same functional form within the framework of the WALE model. That is:

$$\tau_{ij} - \frac{1}{3}\tau_{kk}\delta_{ij} = -2(C_W \Delta)^2 |\bar{N}_{ij}| \bar{S}_{ij} = -C_W^2 \alpha_{ij} \tag{15}$$

$$T_{ij} - \frac{1}{3}T_{kk}\delta_{ij} = -2(C_W \widehat{\Delta})^2 |\widehat{\bar{N}}_{ij}| \widehat{\bar{S}}_{ij} = -C_W^2 \beta_{ij} \tag{16}$$

Using the trio of Eqs. (14)–(16), we subsequently obtain:

$$L_{ij} - \frac{1}{3}L_{kk}\delta_{ij} = -C_W^2 (\beta_{ij} - \widehat{\alpha}_{ij}) \tag{17}$$

In order to solve for C_W, we minimize the square of the error E_{ij} defined by:

$$E_{ij} = L_{ij} - \frac{1}{3}L_{kk}\delta_{ij} + C_W^2 (\beta_{ij} - \widehat{\alpha}_{ij}) \tag{18}$$

Correspondingly,

$$\frac{\partial (E_{ij})^2}{\partial C_W^2} = 0 \tag{19}$$

The dynamic coefficient $C_W^2(x, y, z, t)$ is thereby obtained by the expression:

$$C_W^2 = -\frac{(\beta_{ij} - \widehat{\alpha}_{ij}) L_{ij}}{(\beta_{ij} - \widehat{\alpha}_{ij})(\beta_{ij} - \widehat{\alpha}_{ij})} \tag{20}$$

At this stage, an important feature worth stressing is that the coefficient calculation is based on the local information. However, the values for C_W must usually be limited in order to prevent destabilizing negative viscosity as cited in [26]. Developing a dynamic version of the WALE model was also discussed in [35]. The authors studied the case of an isothermal turbulent channel flow. Their study illustrates how the dynamic procedure combined with the WALE fails to correctly model the mean velocity. It leads to very high values of the WALE constant near the wall and to an over prediction of the turbulent viscosity in the buffer-layer. The authors proposed a cure to this problem using an appropriate dynamic WALE model. For our numerical simulations, we just chose to clip the model constant as commonly used in practice. The following criterion was then imposed: $0 \leqslant C_W \leqslant 0.50$. It should be pointed out that several methods can be used to avoid clipping the local dynamic constant. For relevant studies on the topic one can refer to Refs. [36,37].

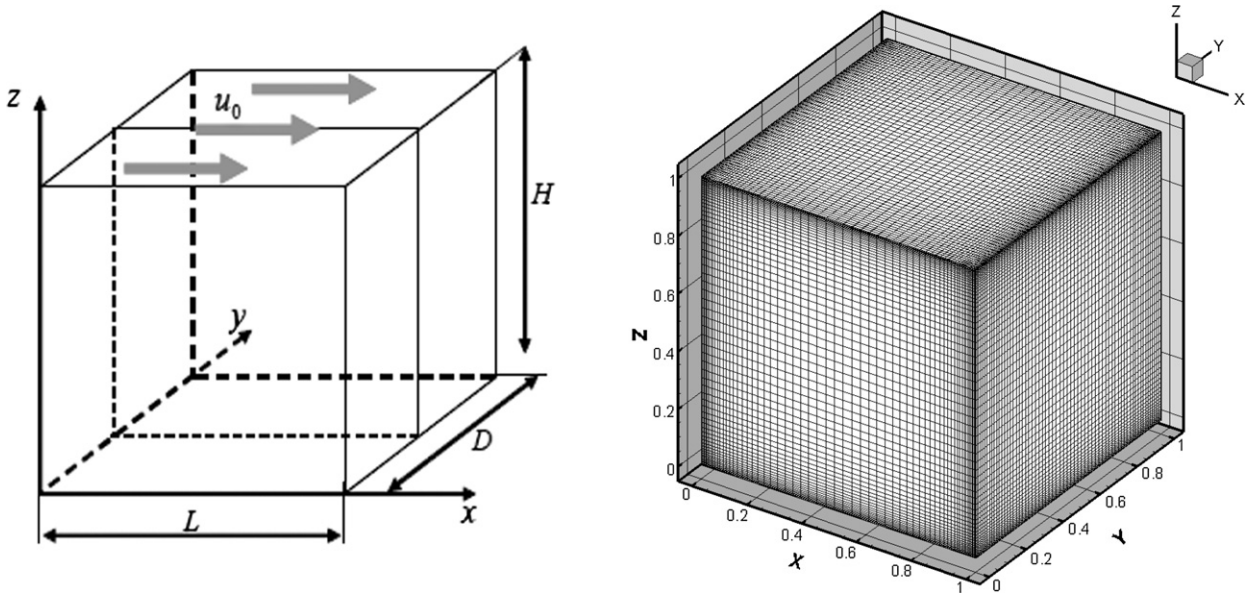

Fig. 1. Geometry of lid-driven cubic cavity problem (left) and the 64^3 grid distribution (right).

3. Numerical procedure

The unsteady Navier–Stokes equations are discretized using staggered, non-uniform control volumes. A projection method attributed to Achdou and Guermond [13] is used to adequately couple the momentum and continuity equations. An intermediate velocity is first computed and later updated to comply with mass continuity. In the intermediate velocity field, the old pressure is used. A Poisson equation, with the divergence of the intermediate velocity field as the source term, is then solved to obtain the pressure correction and afterward the real velocity field. The time evolution terms are discretized with an implicit second-order Euler scheme utilizing

$$\left(\frac{\partial u_i}{\partial t}\right)^{n+1} = \frac{3u_i^{n+1} - 4u_i^n + u_i^{n-1}}{2\Delta t} \tag{21}$$

The advection terms are discretized with an explicit scheme, i.e.,

$$\frac{\partial}{\partial x_j}(u_i u_j)^{n+1} = 2\frac{\partial}{\partial x_j}(u_i u_j)^n - \frac{\partial}{\partial x_j}(u_i u_j)^{n-1} \tag{22}$$

The diffusion terms are treated implicitly and the SGS stresses are discretized with a semi-explicit scheme:

$$\frac{\partial}{\partial x_j}\left[\nu_T\left(\frac{\partial \bar{u}_i}{\partial x_j} + \frac{\partial \bar{u}_j}{\partial x_i}\right)\right]^{n+1} = \frac{\partial}{\partial x_j}\left\{\left(2\nu_T^n - \nu_T^{n-1}\right)\left[\left(\frac{\partial \bar{u}_i}{\partial x_j}\right)^{n+1} + 2\left(\frac{\partial \bar{u}_j}{\partial x_i}\right)^n - \left(\frac{\partial \bar{u}_j}{\partial x_i}\right)^{n-1}\right]\right\} \tag{23}$$

The finite-volume method devised by Patankar [27] is employed to discretize the Navier–Stokes equations. The advective terms in the momentum equation are discretized using a QUICK third-order scheme proposed by Leonard [28]. The discretized momentum equations are eventually resolved using the red and black successive over relaxation method RBSOR (Leonard [29]), while the Poisson pressure correction equation is solved using a full multi-grid method [30,31]. The numerical methodology was implemented with a FORTRAN program. The convergence of the numerical results is established at each time step according to the following criteria:

$$\sqrt{\left(\sum_{I,J,K}(u_i)_{I,J,K}^m - \sum_{I,J,K}(u_i)_{I,J,K}^{m-1}\right)^2} \leqslant 10^{-7} \tag{24}$$

where m represents the iteration level.

4. Results and discussion

4.1. Validation of numerical method

A benchmark test, configured in the form of a lid-driven cubical cavity is illustrated in Fig. 1. Being simple in geometry while exhibiting complex flow behavior, this problem constitutes an ideal setting to benchmark the developed LES computer

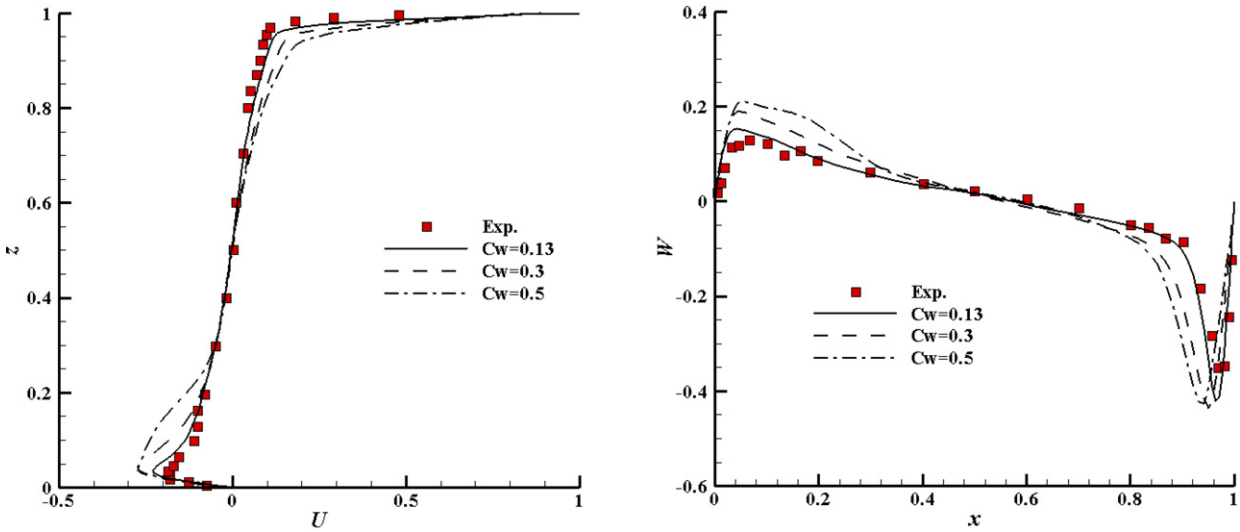

Fig. 2. Comparisons of the mean U (left) and W (right) velocity profiles between the present numerical and experimental results for $Re = 10^4$ and different values of C_W.

code. The Reynolds number is based on the cavity top wall and the impressed lid velocity leading to $Re = \frac{u_0 L}{\nu}$. On the basis of $Re = 10^4$, numerical calculations were performed in a cubic domain ($D = H = L$), containing a total of $64 \times 64 \times 64$ nodes, which are shown in Fig. 1. For completeness, the grids were built using a tangent hyperbolic formulation.

The smallest space intervals chosen in the three coordinate directions are localized near the moving and stationary walls to capture the growth of the velocity boundary layers adjacent to them. For $Re = 10^4$, the largest dimensionless time step to ensure convergence and stability was set at $\Delta t = 2.0 \times 10^{-3}$.

The velocity boundary conditions are:

- $z = 1$: at the moving top wall ($u = 1$, $v = w = 0$)
- $x = 0$, $x = 1$, $y = 0$, $y = 1$, $z = 0$: no slip ($u = v = w = 0$) at the stationary walls.

The statistical analysis of the turbulence quantities was performed taking the velocity field data corresponding to central horizontal and vertical lines in the plane of symmetry ($y = 0.5$). The dimensionless mean velocity components on the two lines defined previously were calculated with the following expressions: $U = \langle \bar{u} \rangle$ and $W = \langle \bar{w} \rangle$, where $\langle \bar{u} \rangle$ and $\langle \bar{w} \rangle$ are mean velocity components in the x- and z-directions, respectively.

Taking into account the Reynolds hypothesis, the instantaneous velocity can be separated into its mean value and a fluctuating part. Consequently, this may be written as follows: $\bar{u}_i = \langle \bar{u}_i \rangle + \bar{u}'_i$, where $\bar{u}'_i$ is the fluctuating part.

The turbulence intensities are defined by the following dimensionless expressions:

$$U_{rms} = 10\sqrt{\langle (\bar{u}')^2 \rangle} \quad \text{and} \quad W_{rms} = 10\sqrt{\langle (\bar{w}')^2 \rangle} \tag{25}$$

The dimensionless Reynolds stress components are given by:

$$UW = 500\sqrt{\langle \bar{u}' \bar{w}' \rangle} \tag{26}$$

Note that the two constants 10 and 500 in the previous expressions were used to amplify the values of the turbulence intensity and Reynolds stress in order to get a suitable graphical representation [16].

Simulations were first carried on with the WALE sub-grid scale model and with a value of $C_W = 0.50$ as proposed in [9]. Note that in [9], the physical problem corresponds to turbulent pipe flow. Data for the present statistical analysis of turbulence were obtained storing the values of all variables corresponding to the centerlines in the horizontal and vertical directions at the symmetry plane; this was done for each time interval.

Fig. 2 displays the dimensionless average velocity components U and W at the centerlines of the symmetry plane. As seen here, the obtained solutions are not in very good agreement with the experimental results of Prasad and Koseff [16]. Another test was then done with a lower value of WALE's constant, say $C_W = 0.30$. Under these circumstances, better results are observable in Fig. 2 demonstrating that the results strongly depend on the value of the constant C_W. As reported by Bricteux et al. [34], the WALE model has an over dissipative behavior in strong vortical flows. Since lid-driven cavities are dominated by large scales vortices, it is probably the reason for the mitigate results observed in Fig. 2.

In order to determine the most appropriate value of the coefficient C_W, we used the DSGS model, which was defined and developed in Section 2. From the standpoint of CPU time, this model is relatively expensive. Hence, simulations were

Table 1
Time/iteration on single processor using different models on a 64^3 grid.

Model	Time (s)
UDNS	0.750
SGS	1.99
DSGS	5.27

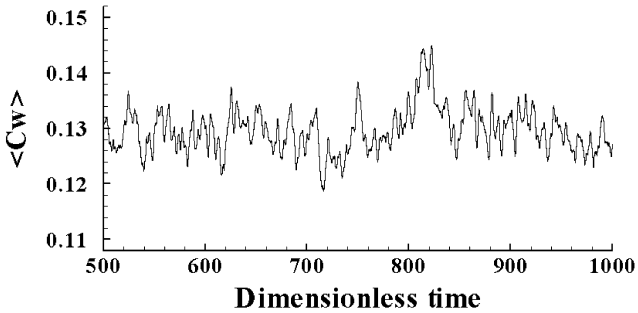

Fig. 3. Time evolution of the space averaged coefficient C_W.

undertaken on a smaller grid size consisting of $48 \times 48 \times 48$ nodes. The coefficient model was then calculated by means of Eq. (21). Table 1 lists the CPU times for one iteration using different models on a single processor, 3.0 GHz Sun Ultra 40 workstation. The SGS model requires approximately 166% more time compared to the UDNS, while the DSGS model takes almost 165% more clock-time compared to the SGS model and 600% compared to the UDNS.

Fig. 3 shows the time evolution of the space averaged value of C_W over the computational domain for Reynolds number $Re = 10^4$. The time averaged value of $\langle C_W \rangle$ in the interval $500 \leqslant t \leqslant 1000$ gave a value of an optimal WALE constant $C_W^{opt} = 0.1297$. It is important to notice that averaging $\langle C_W \rangle$ in a shorter interval, i.e., $500 \leqslant t \leqslant 600$ also gives a very close value: $C_W^{opt} = 0.1291$. Hence, in order to evaluate C_W^{opt} with the DSGS model, there is no need for long integration times.

Fig. 4 displays the results performed on a $64 \times 64 \times 64$ grid using the SGS model with the evaluated optimal coefficient $C_W^{opt} = 0.13$ (obtained with the DSGS model on a $48 \times 48 \times 48$ grid). In this figure are presented the dimensionless mean square root values at the centerlines of the symmetry plane (U_{rms} and W_{rms}), and the dimensionless Reynolds Stresses (UW). Results are compared to experimental measurements in [16], numerical simulations with DNS [18] and LES [22]. The excellent agreement lends credibility to the present methodology for predicting turbulent flow characterized by $Re = 10^4$.

4.2. Flow structure for $Re = 10^4$

On the left part of Fig. 5, we plotted the instantaneous velocity vector field at the x–z midplane in the lid-driven cavity. We recall that the top lid is moving from left to right at a given velocity u_0. A main primary vortex near the cavity center is clearly seen in the figure. The plotted vectors clearly reveal the presence of secondary eddies near the bottom corners namely called upstream and downstream secondary eddies. An upper secondary eddy is also observed on the left of the lid.

The right part of Fig. 5 exhibits the instantaneous vector field in the y–z plane at a location near the downstream wall, specifically $x = 0.84$. Two pairs of Taylor–Gortler–like (TGL) vortices and lower corner vortices are well formed, precluding the possibility of a two-dimensional flow. Note that the mechanism causing the TGL vortices is due to the unstable concave free shear layer that separates the primary vortex from the downstream secondary eddy. The right part of Fig. 5 also brings forth the presence of corner eddies that originate from the no-slip condition imposed by the presence of the end-wall. These visualizations of TGL and corner vortices are in good agreement with the observations in [16].

Some iso-surfaces of x-direction vorticity are plotted in Fig. 6. The iso-surfaces are plotted near the downstream wall at same location as in Fig. 5, $x = 0.84$. Here again, the transitional behavior of TGL and the corner vortices are palpable.

4.3. Optimal WALE constants prediction for higher Reynolds numbers

By increasing the Reynolds number up to 2×10^4, the numerical results explode after a dimensionless time of about 800 even by largely decreasing the time steps. This is certainly due to the boundary velocity imposed on the cavity lid. Indeed, the unit velocity induces severe discontinuities along the two top edges. In order to remove these defects, we used the same high degree polynomial velocity profile employed by Leriche and Gavrilakis [18]:

$$u(x, y, L) = u_0 \left[1 - \left(\frac{2x - L}{L} \right)^{18} \right]^2 \left[1 - \left(\frac{2y - L}{L} \right)^{18} \right]^2 \tag{27}$$

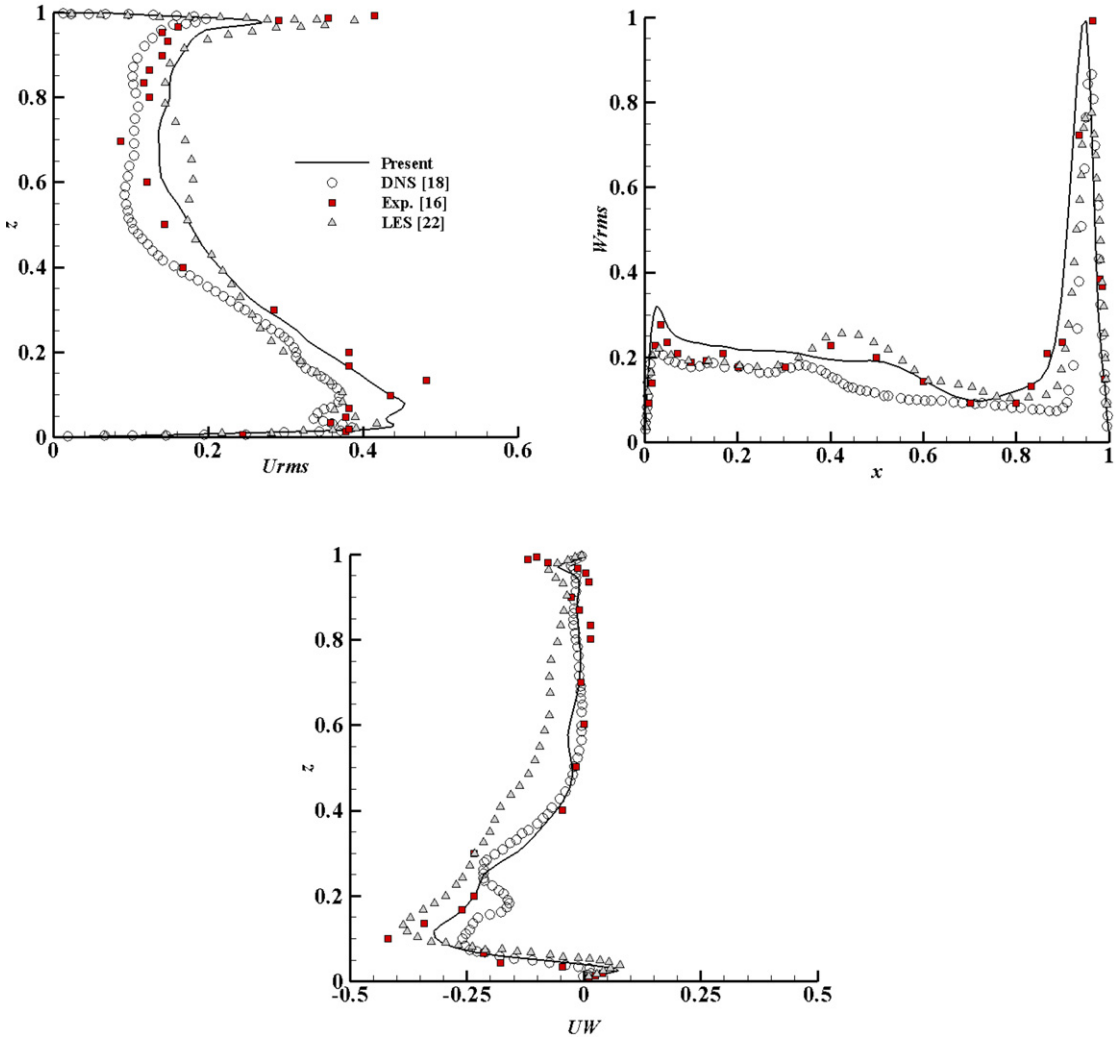

Fig. 4. Comparisons of *rms U* and *W* velocity profiles (top) and Reynolds shear stress profile (bottom) for $Re = 10^4$ between present and DNS, LES and experimental results found in the literature.

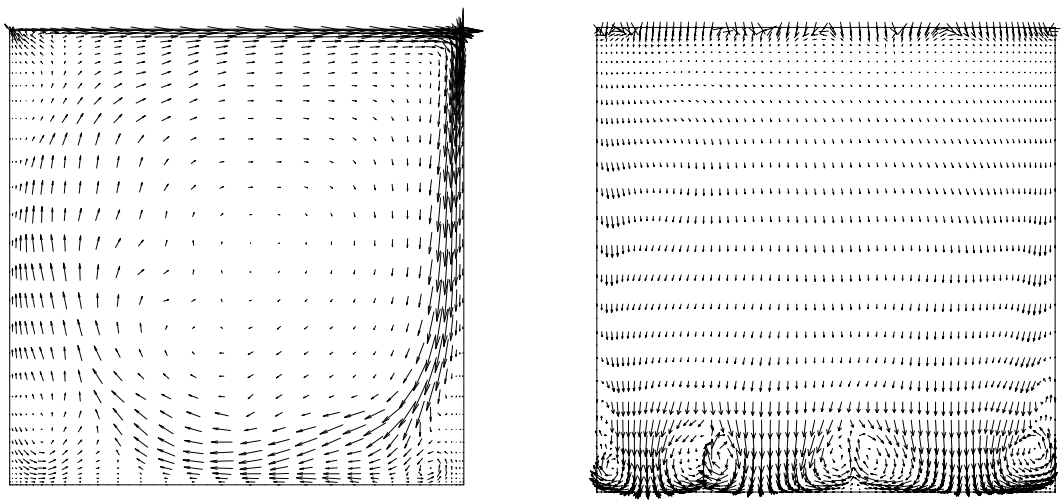

Fig. 5. Instantaneous velocity vectors at *x–z* midplane (left) and *y–z* plane at a location near the downstream wall (right).

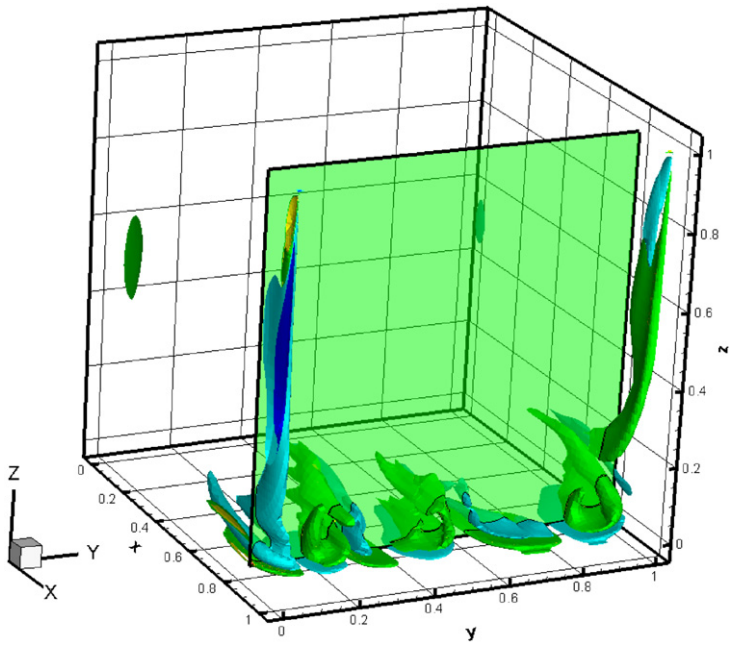

Fig. 6. x-vorticity iso-surfaces near the downstream wall.

Table 2
Time steps and optimal values of C_W related to the Reynolds number.

Re	12 000	18 000	24 000	30 000	36 000
Re_m	10 200	15 300	20 400	25 500	30 600
Δt	2×10^{-3}	1×10^{-3}	1×10^{-3}	5×10^{-4}	2.5×10^{-4}
C_W^{opt} (calculated on a 64^3 grid)	0.132	0.149	0.163	0.175	0.185

Table 3
Smallest and largest space intervals in the three coordinate directions.

$\Delta x_{\min}$	$\Delta x_{\max}$	$\Delta y_{\min}$	$\Delta y_{\max}$	$\Delta z_{\min}$	$\Delta z_{\max}$
2.6×10^{-3}	3.2×10^{-2}	1.0×10^{-2}	1.9×10^{-2}	2.6×10^{-3}	3.2×10^{-2}

In this velocity distribution, the mean value over the driving surface results in $u_m = 0.85u_0$ [18]. Hence, for a Reynolds number based on the maximum velocity on the lid defined by $Re = \frac{u_0 L}{\nu}$, the corresponding mean velocity Reynolds number is defined by $Re_m = \frac{u_m L}{\nu}$. In Table 2 different values of Re and their corresponding Re_m are reported.

In order to solve the optimal WALE coefficient C_W^{opt} for each envisaged Reynolds number, simulations were all performed on a $64 \times 64 \times 64$ grid. The grid distribution responded to the non-dimensional variable x expressed by:

$$x(i) = \frac{1}{2} + \frac{\tanh[(\frac{2i}{M} - 1)\arctan h(\alpha_x)]}{2\alpha_x} \tag{28}$$

where the boundary values are: $x(0) = 0$ and $x(M) = 1$ being α_x a stretching parameter. Similar expressions have been generated for the grid distribution along y and z directions with stretching parameters α_y and α_z, respectively. The presented results were obtained with $\alpha_x = \alpha_z = 0.96$ and $\alpha_y = 0.7$. The smallest and largest space intervals in the three coordinate directions are regrouped in Table 3.

The initial flow conditions for each simulation were the final flow state of the right previous run. For each run, simulations were first performed with the SGS model until establishment of the flow (a total dimensionless time of 1000). After that, simulations were carried out with the DSGS model. As mentioned in Section 4.1, short integration times are sufficient to obtain a good approximation for the coefficient C_W^{opt}. The mean values in space of coefficients C_W were then averaged over time inside the intervals $200 \leqslant t \leqslant 300$ or $100 \leqslant t \leqslant 200$ depending on the Reynolds number. Note that for $Re = 3.6 \times 10^4$, a total dimensionless time of 100 requires 4×10^5 time step iterations. This necessitates approximately 3 weeks of CPU time.

Computed values of C_W^{opt} for the different Reynolds numbers are reported jointly in Table 2 and in Fig. 7. It is important to realize that for $Re_m = 10\,200$, the value of C_W^{opt} is very close to one obtained in a grid with the same Reynolds number.

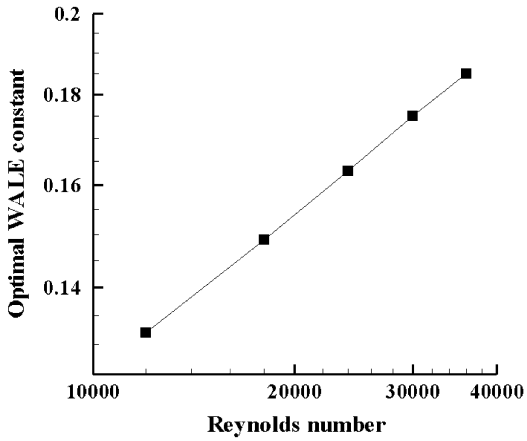

Fig. 7. Optimal WALE model constant versus Reynolds number.

Thus, C_W^{opt} is not very sensitive to the grid size and can be evaluated on a relatively coarse grid by the DSGS model firstly and secondly using a finer grid with the SGS model. For more details about the effect of the grid spacing and integral scale on the constant of SGS models, one can refer to [38].

It was also corroborated that C_W^{opt} can be correlated with Reynolds number Re as seen in Fig. 7. Using the least square method, the optimal value of the constant inherent to the WALE model is expressed by the following correlation:

$$C_W^{opt} = 7.29 \times 10^{-3} Re^{0.308} \tag{29}$$

5. Conclusions

The three-dimensional classical problem of turbulent flows in lid-driven cubical cavities was simulated with a finite volume Large Eddy Simulation methodology in this work. Two sub-grid scale models were implemented, the WALE's (SGS) and the corresponding eddy viscosity dynamic model (DSGS). The results with the SGS model are very coherent with experimental and numerical data from other authors if an appropriate model constant C_W is accounted for.

Optimal values of C_W were obtained by averaging in time the stored data of the space averaged values of $\langle C_W \rangle$ calculated with the DSGS model. For $Re = 10^4$, an optimal value $C_W^{opt} \approx 0.13$ was determined. No significant changes were observed between values of C_W^{opt} obtained on $48 \times 48 \times 48$ and $64 \times 64 \times 64$ grids.

Using the DSGS model on a $64 \times 64 \times 64$ grid, optimal values of C_W for relatively high Reynolds numbers in the interval $10^4 < Re \leqslant 3 \times 10^4$, were adequately determined. A monomial correlation between C_W^{opt} and Re was determined by the least square method. This correlation may be very useful for numerical simulations using the SGS model with higher Reynolds numbers that demand finer grids.

References

[1] M. Henkes, C.J. Hoogendoorn, Natural convection flow in a square cavity calculated with low-Reynolds-number turbulence models, Int. J. Heat Mass Transfer 34 (1991) 377–388.
[2] L. Lijun, L. Jun, F. Zhenping, A numerical method for simulation of attached cavitation flows, Int. J. Numer. Methods Fluids 52 (2006) 639–658.
[3] K. Kim, A.I. Sirviente, R.F. Beck, The complementary RANS equations for the simulation of viscous flows, Int. J. Numer. Methods Fluids 48 (2005) 199–229.
[4] H. Raiesi, U. Piomelli, A. Pollard, Evaluation of turbulence models using direct numerical and large-eddy simulation data, J. Fluids Eng. 133 (2011).
[5] P. Sagaut, Large-Eddy Simulations for Incompressible Flows: An Introduction, Springer, Berlin, Germany, 2001.
[6] J.S. Smagorinsky, General circulation experiments with the primitive equations: I. The basic experiment, Mon. Weather Rev. 91 (1963) 99–136.
[7] M. Germano, U. Piomelli, P. Moin, W.H. Cabot, A dynamic subgrid-scale eddy viscosity model, Phys. Fluids A 3 (1991) 1760–1765.
[8] D.K. Lilly, A proposed modification of the Germano subgrid-scale closure method, Phys. Fluids A 4 (1992) 633–635.
[9] F. Nicoud, F. Ducros, Subgrid-scale modelling based on the square of the velocity gradient tensor, Flow Turbul. Combust. 62 (3) (1999) 183–200.
[10] M. Lesieur, O. Metais, P. Comte, Large Eddy Simulation of Turbulence, Cambridge University Press, London, England, 2005.
[11] B. Ben-Beya, Simulation numérique d'un écoulement bidimensionnel en aval d'une marche descendante, PhD Thesis, Faculty of Sciences of Tunis, El-Manar II, Tunisia, 1995.
[12] N. Ben-Cheikh, Etude de la convection naturelle laminaire et de l'écoulement turbulent dans une cavité entraînée par simulation des grandes échelles, PhD Thesis, Faculty of Sciences of Tunis, El-Manar II, Tunisia, 2008.
[13] Y. Achdou, J.L. Guermond, Convergence analysis of a finite element projection Lagrange–Galerkin method for the incompressible Navier–Stokes equations, SIAM J. Numer. Anal. 37 (2000) 799–826.
[14] M. Germano, U. Piomelli, P. Moin, W.H. Cabot, A dynamic subgrid-scale eddy viscosity model, Phys. Fluids A 7 (1991) 1760–1765.
[15] J.R. Koseff, R.L. Street, The lid-driven cavity flow: a synthesis of qualitative and quantitative observations, J. Fluid Mech. 106 (1984) 390–398.
[16] A.K. Prasad, J. Koseff, Reynolds number and end-wall effects on a lid-driven cavity flow, Phys. Fluids A 1 (1989) 208–218.
[17] A. Yeckel, J.W. Smith, J.J. Derby, Parallel finite element calculation of flow in a three-dimensional lid-driven cavity using the CM-5 and T3D, Int. J. Numer. Methods Fluids 24 (1997) 1449–1461.

[18] E. Leriche, S. Gavrilakis, Direct numerical simulation of the flow in a lid-driven cubical cavity, Phys. Fluids 12 (2000) 1363–1376.
[19] E. Leriche, Direct numerical simulation in a lid-driven cubical cavity at high Reynolds number by a Chebyshev spectral method, J. Sci. Comput. 27 (2006) 335–345.
[20] R. Bouffanais, M. Deville, P. Fischer, E. Leriche, D. Weill, Large-eddy simulation of the lid-driven cubic cavity flow by the spectral element method, J. Sci. Comput. 27 (2006) 151–162.
[21] R. Bouffanais, M. Deville, E. Leriche, Large-eddy simulation of the flow in a lid-driven cubical cavity, Phys. Fluids 19 (2007) 1–20.
[22] J.L. Guermond, P.D. Minev, Start-up flow in a three-dimensional lid-driven cavity by means of a massively parallel direction splitting algorithm, Int. J. Numer. Methods Fluids 68 (2012) 856–871.
[23] A.A. Wray, J.C.R. Hunt, Algorithms for classification of turbulent structures, in: Proceedings of the IUTAM Symposium on Topological Fluid Mechanics, 1989, pp. 95–104.
[24] J. Deardoff, The use of sub-grid transport equations in a three-dimensional model of atmospheric turbulence, J. Fluids Eng. 95 (1973) 429–438.
[25] A. Scotti, C. Meneveau, D.K. Lilly, Generalized Smagorinsky model for anisotropic grids, Phys. Fluids A 5 (1993) 2306–2308.
[26] U. Piomelli, J. Liu, Large-eddy simulation of rotating channel flows using a localized dynamic model, Phys. Fluids 7 (4) (1995) 839–848.
[27] S.V. Patankar, Numerical Heat Transfer and Fluid Flow, McGraw–Hill, New York, 1980, pp. 113–137.
[28] B.P. Leonard, A stable and accurate convective modelling procedure based on quadratic upstream interpolation, Comput. Methods Appl. Mech. Eng. 19 (1979) 59–98.
[29] B.P. Leonard, Templates for the Solution of Linear Systems: Building Blocks for Iterative Methods, SIAM, Philadelphia, PA, USA, 1994.
[30] N. Ben-Cheikh, B. Ben-Beya, T. Lili, Benchmark solution for time-dependent natural convection flows with an accelerated full-multigrid method, Numer. Heat Transf. B 52 (2007) 131–151.
[31] G.A. Gerolymos, I. Vallet, Robust implicit multigrid Reynolds–Stress model computation of 3D turbomachinery flows, J. Fluids Eng. 129 (2007).
[32] T.T. Brandt, Usability of explicit filtering in large eddy simulation with a low-order numerical scheme and different subgrid-scale models, Int. J. Numer. Methods Fluids 57 (2008) 905–928.
[33] G. Zhaolin, J. Jianying, Z. Yunwei, S. Junwei, Large eddy simulation using a dynamic mixing length subgrid-scale model, Int. J. Numer. Methods Fluids 69 (2012) 1457–1472.
[34] L. Bricteux, M. Duponcheel, G. Winckelmans, S. Junwei, A multiscale subgrid model for both free vortex flows and wall-bounded flow, Phys. Fluids 21 (2009) 105102/1–105102/12.
[35] H. Baya Toda, K. Truffin, F. Nicoud, Is the dynamic procedure appropriate for all SGS models?, in: J.C.F. Pereira, A. Sequeira (Eds.), V European Conference on Computational Fluid Dynamics, ECCOMAS, Lisbon, Portugal, June 2010, pp. 14–17.
[36] J. Lee, H. Choi, N. Park, Dynamic global model for large eddy simulation of transient flow, Phys. Fluids 22 (2010) 075106.
[37] F. Nicoud, H. Baya Toda, O. Cabrit, S. Bose, J. Lee, Using singular values to build a sub-grid scale model for large eddy simulations, Phys. Fluids 23 (2011) 085106.
[38] J. Meyers, P. Sagaut, On the model coefficients for the standard and the variational multi-scale Smagorinsky model, J. Fluid Mech. 569 (2006) 287319.